Evaluation of the Relative Neutronic Risk of Alternative Fusion Fuels

by

Joseph Jerkins

Submitted to the Department of Nuclear Science and Engineering
in partial fulfillment of the requirements for the degree of

Bachelor of Science in Nuclear Science and Engineering

at the

MASSACHUSETTS INSTITUTE OF TECHNOLOGY

February 2022

Author .....
Department of Nuclear Science and Engineering
May 20, 2021

Certified by .....
Andrew Hodgdon
Visiting Scientist at PSFC
Thesis Supervisor

Certified by .....
Benoit Forget
Professor of Nuclear Science and Engineering
Thesis Supervisor

Accepted by .....
Michael Short
Associate Professor of Nuclear Science and Engineering
Chair, NSE Committee for Undergraduate Students

Evaluation of the Relative Neutronic Risk of Alternative Fusion Fuels

by

Joseph Jerkins

Submitted to the Department of Nuclear Science and Engineering
on May 20, 2021, in partial fulfillment of the
requirements for the degree of
Bachelor of Science in Nuclear Science and Engineering

Abstract

The radiological risk profiles of a variety of fusion fuels were assessed, to aid understanding of the influence of fuel choice on the safety and cost of future commercial fusion power plants. Shielding thickness and activation dose rates were modeled for five fusion fuels consisting of Deuterium-Tritium, Deuterium-Deuterium, Deuterium-Helium 3, Deuterium-Lithium 6, and Hydrogen-Boron 11. Simplistic shielding and activation models were carried out in standardized 500MW reactors.

Thesis Supervisor: Andrew Hodgdon
Title: Visiting Scientist at PSFC

Thesis Supervisor: Benoit Forget
Title: Professor of Nuclear Science and Engineering

Acknowledgments

I would like to express my deepest thanks to Andrew for introducing me to the world of neutronics and radiation safety, and for never failing to provide contacts when my research took me outside his area of expertise.

I would like to thank Prof. Forget for providing great intuition regarding the sensitivity of my model to its assumptions and helping me validate them.

Finally, I would like to thank Ethan Peterson and Megan Wart for helping me debug and validate my FISPACT models.

Contents

Chapter 1

Introduction

The demand for energy that is both clean and reliable has prompted many decades of research into nuclear fusion. To this end a variety of approaches have been considered; one such variable is the choice of fuel. The most common fuel considered for fusion is a mixture of the hydrogen isotopes Deuterium and Tritium, and consequently the radiological risk profile of this fuel mix is well understood.

Fusion plasmas composed of Deuterium and Tritium release approximately 80% of their energy in the form of energetic neutrons, which are difficult to harvest energy from due to their high penetrating ability in matter and lack of an electric charge. Additionally, neutrons undergo nuclear reactions with most materials to produce radioactive isotopes that present a safety hazard. Yet another difficulty of Deuterium-Tritium fueled fusion reactors is the lack of natural Tritium; the fuel must be bred using an existing source of neutrons. Because of these difficulties, alternative fuels have long been considered which release energy via charged particles and do not require isotopically enriched fuel.

These fuels typically suffer from lower reactivity and require more extreme physical conditions to achieve fusion, and are thus much less well characterized in experiment and theory. As a result, there is much less data pertaining to the neutron radiation and activation risks of such fuels, leading to uncertainty in aspects of personnel safety and reactor design. Future work on the design and construction of such reactors burning alternative fuels would thus be aided by models of the radiological risks posed.

This thesis models the operational neutron production, leakage, and nuclear activation risk of the most common alternative fusion fuels through a combination of fundamental theory and industry standard modeling software. Approximate neutron flux and spectra for characteristic plasmas, the corresponding structure activation for commonly used materials in fusion reactors, and the required shielding of reactors using these fuels will be presented. The flux/spectra provide a measure of short-term or operational dose risk, while the activation provides a measure representing long-term risk by activation or cumulative/end of life dose rates.

Chapter 2

Background

Fusion research has thus far focused primarily on the reaction of deuterium and tritium (D-T fusion) due to the low temperatures required for ignition and high cross section for reaction. Despite this, alternative fuel mixtures have been long considered attractive due to benefits over other aspects of D-T fusion. These benefits may include giving off energy in easier forms to capture than neutron radiation, higher natural abundance, and absence of a need for enrichment or tritium breeding in the fuel cycle.

In the case of most alternative fuels, the primary energy producing reaction is "aneutronic" in that no neutrons are produced and the majority of energy is released into ions instead. This is highly preferable from the perspective of radiological safety, as neutron radiation tends to lead to the greatest material activation compared to high energy ions or photons. Additionally, the charged nature of ions formed in aneutronic reactions is convenient when converting fusion energy into electricity. Rather than a traditional thermodynamic cycle, their energy may be harnessed by direct energy conversion methods such as electrostatic potentials or induction[15][11]. Fusion reactors using aneutronic fuels are thus potentially more efficient than traditional D-T reactors.

2.1 Physics

Unfortunately, many fuel mixtures have reactions with either a daughter product and one of the primary reactants, or a reaction with lower cross section between the primary reactants which does produce neutrons. The magnitude of neutron production for many alternative fuels is not modeled due to a lack of existing experiments (barring deuterium, which is very frequently used as a substitute for the D-T mix in experimental reactors). Thus, the magnitude of the radiological risks associated with these indirect neutron production pathways is largely unknown. The fuels and corresponding reactions considered in this research are shown in table 2.1:

Table 2.1: Fusion fuel mixtures and their relevant reactions.

Fuel Mixture	Reactions
D,T	$D+T \rightarrow He^4+n$ $D+D \rightarrow He^3+n$
D,D	$D+D \rightarrow He^3+n$ $D+D \rightarrow H+T$
D,He^3	$D+D \rightarrow He^3+n$ $D+He^3 \rightarrow He^4+H$ $D+D \rightarrow H+T$
D,Li^6	$D+Li^6 \rightarrow 2He^4$ $D+Li^6 \rightarrow Be^7+n$ $D+Li^6 \rightarrow He^4+He^3+n$
H,B^{11}	$H+B^{11} \rightarrow 3He^4$ $H+B^{11} \rightarrow C^{11}+n$ $He^4+B^{11} \rightarrow N^{14}+n$

D and T are used as shorthand for H^2 and H^3 respectively, n is used as shorthand for neutrons.

Inclusion for reactions was determined by a survey of known reactions between the fuel mixture components in the ENDF nuclear reaction library[6]. Reactions were considered which produced neutrons or released energy in excess of 0.1 MeV and had cross sections higher than 10^{-6} barns at an energy equal to the thermal energy of the fusion plasma. For all of the Deuterium-based fuel mixes listed above, this sufficiently captured the power and neutron production such that inclusion of reactions with lower cross section did not qualitatively change the magnitude of either quantity. In the case

of H-B11 as a fuel however, there are no neutron-producing reactions with such a high cross section between the primary reactants. The two neutron-producing reactions with highest cross section and thus the greatest neutron production rate were thus considered, as listed in table 2.1.

2.1.1 Nuclear Properties

The ultimate neutron production rate for each fuel depends on the reaction rate, which is in turn dependent on free parameters that are set by the plasma physics of the reactor burning it. There is thus a need to independently determine what the relevant plasma parameters are for each fuel, so that a comparison between them with the intent of quantifying their relative risk in a power generation scenario is meaningful. To do this, it is first necessary to identify all power producing and neutron producing reactions that occur in a fusion plasma composed of each fuel mixture. For each of these reactions, the relevant physical parameters are the reaction cross section and the so-called Q value or energy released per reaction. Figures B-1 through B-3 show the relevant cross sections for each fuel mix. The Q-values for each reaction are listed below in Table 2.2.

Table 2.2: Q-value of relevant reactions

Reaction	Q (MeV)
$D+T \rightarrow He^4+n$	17.59
$D+D \rightarrow He^3+n$	3.269
$D+D \rightarrow H+T$	4.033
$D+He^3 \rightarrow He^4+H$	18.35
$D+Li^6 \rightarrow 2He^4$	22.37
$D+Li^6 \rightarrow Be^7+n$	3.381
$D+Li^6 \rightarrow He^4+He^3+n$	1.795
$H+B^{11} \rightarrow 3He^4$	8.683
$H+B^{11} \rightarrow C^{11}+n$	-2.766
$He^4+B^{11} \rightarrow N^{14}+n$	0.1574

2.1.2 Neutron Source

Before any neutronic analysis may be performed, the volumetric neutron source rate (neutrons/s) and energy spectrum must be calculated as a function of reactor fuel and the corresponding plasma parameters. This requires evaluating the volumetric reaction rate, which is defined by the velocity space integral over the distribution functions of both fuel species:

$$R_{12} = n_1 n_2 \langle \sigma_r v \rangle \tag{2.1}$$

$$\langle \sigma_r v \rangle = \int f_1(\mathbf{v_1}) f_2(\mathbf{v_2}) \sigma_r(|\mathbf{v_2} - \mathbf{v_1}|) |\mathbf{v_2} - \mathbf{v_1}| d\mathbf{v_1} d\mathbf{v_2} \tag{2.2}$$

where f_i refers to the normalized velocity distribution function of species i, and σ_r refers to the cross section of reaction r as a function of relative velocity. The velocity distribution function is assumed to be Maxwellian for all species:

$$f_i(\mathbf{v}) = \left(\frac{m}{2\pi k_B T} \right)^{3/2} \exp\left(-\frac{m\mathbf{v}^2}{2k_B T} \right) \tag{2.3}$$

For all reactions in this work, a single neutron is produced per reaction and thus the reaction rate is equal to the neutron production rate. In order to compare neutron production between fuels, it is necessary to normalize the neutron production rate to the power produced by the fuel. A useful figure of merit that can be assigned to each fuel mix is thus the ratio of the volumetric neutron production rate R to the power density P (referred to from hereon as the neutron efficiency), given by the sum of all power-producing reaction rates multiplied by their corresponding Q value:

$$\frac{R_{tot}}{P} = \frac{\sum_{r_i} n_{i1} n_{i2} \langle \sigma_{r_i} v \rangle}{\sum_{r_j} n_{j1} n_{j2} \langle \sigma_{r_j} v \rangle Y_j} \tag{2.4}$$

Besides the neutron production rate, it is necessary to calculate the energy distribution or spectrum of the neutrons produced. This is because neutron penetration and neutron-induced activation in matter depend heavily on the energy of the neutron. For this, a similar integral to the rate equation is required, but the relationship

between collision velocity and outgoing neutron energy must be inserted. This requires applying conservation of momentum and conservation of energy to the system of particles. For the sake of clarity, the derivation of this relationship is in Appendix A. The energy dependence for all neutron-producing reactions are shown in Figure B-4. With a relationship between the relative velocity of colliding nuclei and the energy of outgoing neutrons, the spectrum is fully specified given the distribution of velocities of reacting species in the plasma.

2.1.3 Radiation Transport and Material Activation

As neutrons propagate through matter, they scatter and lose energy. These scattering reactions lead to the production of high energy "secondary photons" as the energy absorbed into the matter is radiated away. Because of this phenomenon, the dose caused by a neutron source that has been largely attenuated will be primarily due to photons. It is thus strictly necessary to account for them when modeling the necessary shielding of a reactor.

Neutrons may also react with nuclei in the material to form unstable isotopes, thus inducing short and long-lived radioactivity in structures. This incurs a safety risk and burden to the operation of any fusion reactor which produces neutrons, as entering the reactor for maintenance or decommissioning become hazardous.

It is these two mechanisms which present radiological risk and require modeling. In this work, the Monte Carlo N-Particle (MCNP) transport code is used to calculate the change in neutron energy spectrum and flux due to material interaction[8], as well as the ambient radiation dose during full power operation of a reactor burning each fuel. Both neutrons and the secondary photons they produce are simulated to model the relationship between shielding and dose rate.

To calculate the activation of reactor structures given incident neutron flux and spectrum, the FISPACT-II inventory code is used[17]. FISPACT-II computes the reaction rate of every nuclear transmutation reaction that occurs in a given material under neutron irradiation, based on the neutron spectrum/flux and the material composition and density. Given a duration of irradiation, this results in a new material

composition and a corresponding level of induced radioactivity. FISPACT is also used to track the decrease in activity over time after irradiation ceases, due to decay of radioisotopes.

The rate of change of the amount of a material due to incident neutron radiation and decay losses/gains is expressed via the following ODE which FISPACT-II solves:

$$\frac{dN_i}{dt} = \sum_j (\lambda_i^j + \sigma_i^j \phi) N_j \tag{2.5}$$

Here, N_i is the number of nuclei i present, N_j is the number of nuclei j, λ_i^j is the decay constant for nucleus j to decay into nucleus i, σ_i^j is the cross section for nuclear transmutation of species j into i, and ϕ is the incident neutron flux. For $j = i$, λ_i^j and σ_i^j represent the total decay constant and cross section for all reactions decreasing N_i and are negative. The composition of a given material sets all N_i and N_j, while the physical properties of these nuclides correspond to λ_i^j and σ_i^j. This system of coupled equations is expressed as a directed graph and solved via Gear's method for systems of stiff differential equations[9].

2.2 Materials

Because fusion reactor designs use a wide variety of materials on the plasma facing side, the radiological analysis of this work is run multiple times per fuel on different potential materials for the first wall. A list of fusion-relevant materials was chosen from the PNNL materials compendium [18], and is shown below in Table 2.3.

Table 2.3: Materials used in reactor model

Material	Location
Beryllium	First Wall
Boron Carbide	First Wall
Graphite	First Wall
Mo-TZM	First Wall
Tungsten	First Wall
Inconel-625	Vacuum Vessel
SS 316L	Vacuum Vessel/Structure
Concrete	Shielding

Chapter 3

Methods

In order to meaningfully compare the radiological risks of various fuels, this analysis adopts a standard reactor model which abstracts as many potential differences in implementation between power reactors using each fuel as possible. Factors such as geometry and design power are standardized and simplified, while the unique nuclear and plasma physics of each fuel are used to set the plasma parameters which in turn set reactor size. This model takes in physical constants for each candidate fuel mixture such as reaction cross section and Q value, and uses these to determine plasma parameters such as temperature and density. The two most direct consequences of radiological risk—and thus the most relevant when comparing fuel types—are the induced activity of the reactor structure, and the amount of shielding required around the reactor to obey regulatory limits on operational dose.

Calculating these requires a chain of simulation codes. First, starting from physical properties of each fuel the neutron production rates and energy spectra are found via the method outlined in the previous section and Appendix A. To evaluate the fusion reaction rates in the plasma and the corresponding emitted neutron spectra, a Monte Carlo integration scheme is used. The flux and spectra are then input to MCNP, which outputs the change in spectrum and integral flux due to scattering and absorption throughout the reactor and shield. FISPACT is then used to calculate material activation of the model reactor. The computational pipeline consisting of these methods to generate neutron flux and material activations is shown in Figure

B-5.

3.1 Plasma Assumptions

For all fuels considered, the plasma is assumed to be isotropic and uniform. A plasma density of $n = 10^{20}$ m^{-3} is used, as this is close to the operational density for a wide variety of modern plant-scale proposed reactor designs.[1] The density ratio of fuel nuclei and the operational plasma temperature are chosen to maximize reactivity as previously determined in literature. For D-T, a fuel mixture of 50%-50% D-T and a temperature of 13keV are assumed[10]. For D-D, a temperature of 70keV is assumed[16]. For D-He3, a fuel mixture of 50%-50% and an optimal temperature of 70keV are assumed[16]. For D-Li6, a fuel mixture of 50%-50% and a temperature of 300keV are assumed.

For H-B11, the most prominent neutron-producing reaction is not due to either of the primary reactants but due to the B11(He4,n)N14 side reaction. For this plasma, a helium ash concentration of 5% is assumed as in [13] based on calculated acceptable limits for $Q \geq 20$, and the helium population is conservatively assumed to be fully thermalized to 300keV. For the remaining 95% of the plasma, an optimal fuel mixture of 85%-15% B11-H and a temperature of 300keV are assumed[12]. Of note, because the cross section for the neutron-producing side reaction has a strong positive dependence on energy well into the MeV range as shown in figure B-3, the reaction rate and neutron spectrum for this reaction are both underestimated in this work.

3.2 Monte Carlo Integrator

In general, the $\langle \sigma_r v \rangle$ integral is not analytic. It can be analytically solved in the case of Maxwellian distributions and simple analytic fits for the cross section, but this requires a unique analytic form for the cross section. Manual integration is made difficult due to the high dimensionality of the integrand; integrating over six

[1] See [4] and [7] for proposed D-T power reactor plasma densities, and [13] for H-B11.

velocity components leads to very slow convergence for traditional quadrature-based integration schemes. For these reasons, a Monte Carlo code is used to calculate the $\langle \sigma_r v \rangle$ integral for all fuels.

Monte Carlo integration is a statistical approximation method performed by drawing random samples within the domain of integration in an attempt to fully measure the volume of the integral. For an integral over the domain D, the Monte Carlo evaluation can be written as

$$\int_D f(x)dx \approx \frac{1}{N} \sum_N f(X) \tag{3.1}$$

Where N samples of X are drawn from a distribution spanning the same space as D. To further accelerate convergence of this Monte Carlo integration, importance sampling is used. For variables sampled from a nonuniform distribution over D with probability density function p_i, the Monte Carlo integral approximation becomes:

$$\int_D f(x)dx \approx \frac{1}{N} \sum_N \frac{f(X)}{p(X)} \tag{3.2}$$

Applying this to the $\langle \sigma_r v \rangle$ integrand results in the following:

$$\langle \sigma_r v \rangle \approx \frac{1}{N} \sum \frac{f_1(\tilde{v_1})}{p_1(\tilde{v_1})} \frac{f_2(\tilde{v_2})}{p_2(\tilde{v_2})} \sigma_r(|\tilde{v_2} - \tilde{v_1}|)|\tilde{v_2} - \tilde{v_1}| \tag{3.3}$$

A great benefit of this scheme lies in the fact that Maxwellian velocity distributions are a form of Gaussian distribution; if $\tilde{v_1}$ and $\tilde{v_2}$ are directly sampled from a Gaussian identical to the species distribution functions, then the two importance sampling fractions cancel and the Monte Carlo evaluation of the integral becomes more efficient:

$$\langle \sigma_r v \rangle \approx \frac{1}{N} \sum \sigma_r(|\tilde{v_2} - \tilde{v_1}|)|\tilde{v_2} - \tilde{v_1}| \tag{3.4}$$

As discussed in the previous section and in Appendix A, given a pair of velocities one can calculate the outgoing neutron energy. The neutron spectrum can thus be simultaneously approximated with evaluation of $\langle \sigma_r v \rangle$. Sampled velocities are used

to calculate the outgoing neutron energy, which is weighted by the differential $\langle \sigma_r v \rangle$ element corresponding to the pair of velocities and then tallied. All spectra tallied in this work were put into 100 equally sized energy bins, evenly spaced between 0 and 20 MeV.

Once the neutron source activity and spectrum are both calculated, they can be fed into the model reactor in MCNP to calculate attenuation and spectral changes due to scattering in material.

3.3 Model Reactor

To standardize results for comparison, all reactors are designed to output 500MW fusion power. The plasma physics considerations already discussed fully constrain the fusion power density, and thus for a spherical uniform plasma the reactor radius R_r is easily defined:

$$R_r = \left(\frac{3}{4} \frac{0.5\text{GW}}{Q n_1 n_2 \langle \sigma_r v \rangle} \right)^{\frac{1}{3}} \tag{3.5}$$

The plasma is surrounded by the first wall, assumed 1cm thick as in ITER. Immediately surrounding the first wall is the vacuum vessel, for which a thickness of 5cm was chosen based on ITER and SPARC values[7][4]. Outside of the vacuum vessel, a 30cm layer of steel is used to represent the structural/load-bearing region of the reactor. Finally outside the structural layer, concrete is used as a shield for neutron and photon radiation. To quantify the radiological risk of each fuel, the thickness of this concrete shield was allowed to vary so that a constant regulatory dose rate limit was exactly met at its outer surface. The dose rate was calculated per ANSI/ANS-6.1.1-1991[3] fluence to dose factors, and the thickness is set such that the 10 CFR 20 High Radiation Area designation of 100mR/h at 30cm from the surface of the concrete[1] was met to the nearest cm. A diagram of the shell model is shown in Figure B-6.

3.4 MCNP and FISPACT

All MCNP models were run until the relative error for the 30cm dose value output fell below 0.2. A model was run on an initial guess for the requisite thickness to bring the dose below the regulatory limit, and the dose measured. The thickness was then adjusted to bring the dose closer to the exact value of the limit. This process was repeated until a thickness in even multiples of cm was reached for which decreasing would lead to exceeding the regulatory limit.

After running MCNP on the reactor model and previously calculated neutron source, average fluxes in the first wall, vacuum vessel, and structure were returned and then used to calculate material activation. This final calculation was performed with FISPACT, for estimates of the material activation of the first wall and vacuum vessel of a power reactor. The dose rate observed due to various reactor structures from one year of operation was calculated, to provide rough figures for the risks posed to maintenance and decommissioning efforts. For all FISPACT calculations, the cross section library TENDL-2017[5] was used

Chapter 4

Results

4.1 Neutron Production Rates

Curves showing $\langle \sigma v \rangle$ of all relevant reactions for each plasma as a function of temperature are shown in Figures B-7 to B-9. The first quantity of comparison is the neutron production rate per unit power for each fuel from equation 2.4. These are shown below in Table 4.1, organized from highest to lowest in descending order.

Table 4.1: Neutron Source Characteristics

Fuel Mixture	Neutrons/MJ
D-D	$8.199*10^{17}$
D-Li6	$7.237*10^{17}$
D-T	$3.558*10^{17}$
D-He3	$4.049*10^{16}$
H-B11	$1.024*10^{15}$

In terms of radiological risk in a reactor, the lowest possible neutron/energy is desirable. From this metric, we can see that D-D reactors create the most neutrons per unit energy produced, followed by D-Li6 and D-T. D-D is the greatest neutron source largely due to the low Q-value of both reactions (approx. 3 and 4 MeV).

4.2 Neutron Spectra

The energy dependence of each neutron-producing reaction is shown in Figure B-4. As required by conservation of energy, the outgoing neutron energy is linearly dependent on initial energy of the two reactants. The spectra calculated for each fuel are shown in Figures B-10 to B-12. Most apparent from these figures is the low energy of neutrons from all alternative fuels. While essentially all of the neutrons produced by D-T plasmas have an energy of approximately 14 MeV, the next highest energy peak out of all fuels is that of D-Li6 at approximately 4 MeV. This leads to less penetration and thus less shielding required to mitigate operational dose rate.

It is worth noting that the neutron spectrum in a real H-B11 reactor would likely be of higher average energy, as this analysis assumed alpha particles were in thermal equilibrium with the plasma despite being born at MeV energies. Additionally, as is clear from Figure B-3, alpha particles born at high energy from the primary H-B11 fusion reaction would have a higher cross section for reaction. Due to both of these factors, the figures derived in this work for H-B11 fueled reactors are conservative.

4.3 Reactor Shielding

The power densities of each fuel mixture as well as the neutron source rate and plasma radius at 500MW are shown below in Table 4.2. From these values, a few features are notable. The low power density and correspondingly high plasma radius of D-D fuel leads to the highest neutron source rate out of all fuels. D-He3 produces less than 5% as many neutrons than D-D despite sharing an identical spectrum, due to a much higher power density and lower neutron source rate. D-Li6 is quite similar to D-D, with a higher power density and slightly lower neutron source rate. H-B11 stands out from the other fuels considered, producing just 0.1% as many neutrons as D-D and 0.3% as many as D-T fusion for the same power output.

Using these radii to set the initial reactor size and the thicknesses described in the previous chapter, the concrete thicknesses required to lower operational dose rate

Table 4.2: Physical Parameters of 500MW Reactor

Fuel Mixture	Power Density (MW/m^3)	Neutron Source Rate (n/s)	Plasma Radius (m)
D-D	0.172	$4.10 * 10^{20}$	8.85
D-He3	0.872	$2.02 * 10^{19}$	5.15
D-Li6	0.415	$3.62 * 10^{20}$	6.60
D-T	1.463	$1.78 * 10^{20}$	4.34
H-B11	1.530	$5.12 * 10^{17}$	4.27

below 100mR/h were calculated and are shown below in Table 4.3.

Table 4.3: High Rad. Area Shielding at 500MW

Fuel Mixture	Concrete Thickness (m)
D-T	3.43
D-Li6	3.34
D-D	3.30
D-He3	2.92
H-B11	2.24

Most notable from this figure, all shielding thicknesses are fairly similar despite stronger variation in neutron source rate and spectra. The influence of high energy neutrons from D-T is evident, as it requires the thickest shielding despite producing about half as many neutrons as D-D or D-Li6. Most deuterium-containing fuels have approximately the same shielding needs for identical reactor powers, but D-He3 stands out as requiring a half meter less shielding due to a combination of its high power density and low neutron efficiency. H-B11 is the clear outlier, as expected due to its much lower neutron efficiency.

For all fuels, shielding thickness was found to be independent of first wall material. This can be understood as a consequence of the relative thickness of the first wall versus the radiation shielding, in combination with the mean free path of neutrons. The mean free path λ is defined as the average distance a particle travels between collisions in a given medium and is defined as:

$$\lambda = \sum_i \frac{1}{n_i \sigma_i} \tag{4.1}$$

where n_i are the number densities of each isotope in the material and σ_i is the total cross section for all nuclear interactions between isotope i and the traveling particle. For all first wall materials considered at energies of a few MeV, the mean free path is greater than 1cm and thus the average neutron will not even interact with the first wall.

Before continuing, the relationship between power density and reactor size is worth brief additional discussion due to the inherent differences in the form of energy released by each fuel. The majority of D-T fusion energy (approximately 80%) is carried by neutrons, and thus any system designed to extract energy from a D-T plasma is limited to thermal methods based on capture of neutron energy via scattering. On the other hand, neutrons carry only 1-2% of the energy released in a D-He3 plasma, and approximately 0.05% of the energy released in a H-B11 plasma. In these cases, direct energy conversion methods can be used which take advantage of electromagnetic interactions with efficiencies 10-30% greater than pure thermodynamic cycles[11] for an equivalent electrical output. Because the ultimate goal of a fusion power plant is to produce electrical power, this should roughly translate to a 10-30% reduction in plasma volume (ignoring nonlinear effects due to power profiles in real plasmas) and neutron source rate. The effect on shielding thickness in this case is nearly negligible; scaling the power down by 15% for a H-B11 plasma (chosen as it is the most likely to benefit from direct energy conversion schemes) resulted in a decrease in required shielding of only 2 cm. Thus, while the energy conversion method may have an influence on the economics and size of a reactor running on alternative fuel, the effect on shielding will be small.

4.4 Reactor Structure Activation

Activation studies were run for each fuel on every first wall material, the vacuum vessel, and the structural layer. The reactor was assumed to run at full power for 1 year, to provide baseline activation levels that a utility operating a reactor might expect during the majority of its lifetime. The results for each first wall material (save

for Beryllium, which had no measurable activation for any fuel choice) are shown in figures B-14 through B-17. Activation of the vacuum vessel and structural layer is shown in figures B-18 through B-27. Values reported are in Sv/h for a semi-infinite slab of the activated material.

For Boron Carbide and Graphite first walls, activation was nearly identical between all deuterium-based fuels, while H-B11 produced an activation of approximately one third as much. For TZM and Tungsten first walls, fuel choice had a larger impact, with D-T leading to nearly 3 orders of magnitude more activation than H-B11 fueled reactors.

In the vacuum vessel and support structure, the difference in activation risk is more clear. D-T, D-D, and D-Li6 consistently gave nearly identical activation (values well within same order of magnitude), while D-He3 and H-B11 led to activations lower by consistent factors of 100 to 10000, respectively.

To compare the activation risk on a more practical level, the semi-infinite slab dose rates from the vacuum vessel after 1 month of shutdown are compared in Table 4.4 below. This roughly corresponds to the dose that maintenance workers might observe while working on a power reactor during shutdown, and thus provides a reasonable figure of comparison. All values are reported in the form of dose rate averaged over all values reported per first wall material. For each fuel, the time to reach the annual occupational dose limit[2] is reported as well.

Table 4.4: Approximate Maintenance Dose Rates After One Month Shutdown

Fuel Mixture	Avg. VV Dose Rate (Sv/h)	Time to Annual Limit
D-T	$3.7 * 10^3$	0.05 sec
D-Li6	$3.0 * 10^3$	0.06 sec
D-D	$1.5 * 10^3$	0.12 sec
D-He3	$4.6 * 10^1$	3.90 sec
H-B11	$1.0 * 10^{-1}$	30 min

It is immediately clear from these results that H-B11 reactors have structure activation well below that of reactors burning other fuels. The dose rate for D-T, D-Li6, D-D, and D-He3 are far above any regulatory limit for occupational dose rate

and thus maintenance would be impossible to perform in-person for reactors burning these fuels on a shutdown time of 1 month. In the case of H-B11 the dose rate is still high enough to make maintenance work quite dangerous from a radiological safety perspective, but raises the possibility of such work being viable. If a H-B11 reactor were able to lower the neutron source rate by an order of magnitude through methods such as reducing the helium ash concentration as discussed earlier, then maintenance enters the realm of possibility.

Chapter 5

Conclusions

From all of the above analysis, various aspects of radiological risk are captured. The operational hazard is reflected in the thickness of shielding required to prevent personnel from exceeding regulatory dose limits in a highly simplified reactor model. The maintenance and decommissioning hazards/costs are captured in the dose rate caused by activation of the structure, which is reported over time following a year of full power operation. The feasibility of maintenance on such a reactor is additionally captured by the time to reach an occupational dose limit due to activation of the vacuum vessel.

From the values of neutrons produced per unit energy, it is clear that "aneutronic" fuels are best understood as having less of a neutronic risk, but that the design burden of neutron radiation is always far from negligible no matter the fuel choice. A thousand-fold decrease in neutrons produced by H-B11 reactors corresponds to a 30% reduction in shielding required, demonstrating that the amount of necessary shielding is relatively insensitive to changes in the neutron source strength and ultimately not a driving factor of the reactor design.

The decreases in neutrons are, however, directly related to the activation of the reactor structure. Reactors burning D-T and D-Li6 lead to the most activation, with D-Li6 inducing more activity in the innermost structures than D-T in many cases. D-D typically leads to activation within about a factor of 2 or 3 of the prior two fuels, and thus should not be considered to present a significantly different risk profile in

terms of activation. D-He3 consistently activated structures at a level approximately 10 times lower than the other Deuterium-based fuels and thus more clearly stands out as an attractive choice in terms of low activation. Finally, dose due to structure activation from H-B11 neutrons is shown to be between 100 and 10000 times less than traditional D-T. Of final note, as discussed in Chapter 2 the neutron production rate for H-B11 is heavily dependent on how one models the temperature and concentration of the alpha population. Future work may use more accurate figures for these to better quantify the neutron source rate and levels of activation.

Appendix A

Neutron Energy Spectrum

To calculate the spectrum of neutrons, it is necessary to relate the energy of colliding particles sampled from the plasma species distribution functions to the energy of outgoing electrons. The fusion system corresponds to inelastic scattering and can be modeled by conservation of momentum with two degrees of freedom in the scattering plane, as well as conservation of energy. The coordinate system is chosen to lie in the rest frame of one of the two colliding nuclei, and shown in figure A-1. Conservation of momentum is expressed in terms of the kinetic energies as follows:

$$\sqrt{2m_1E_1} = \sqrt{2m_nE_n}\cos(\theta) + \sqrt{2m_3E_3}\cos(\phi) \tag{A.1}$$

$$\sqrt{2m_nE_n}\sin(\theta) + \sqrt{2m_3E_3}\sin(\phi) = 0 \tag{A.2}$$

Conservation of energy has the simple form:

$$\frac{m_1v_1^2}{2} = \frac{m_nv_n^2}{2} + \frac{m_3v_3^2}{2} \tag{A.3}$$

This is a system of 3 equations with 4 unknowns of v_n,v_3,θ, and ϕ. Because the only quantity of interest is the neutron energy, we can eliminate v_3 and ϕ, write v_n solely as a function of θ, and convert to units of kinetic energy rather than velocity. This

results in the following relationship:

$$E_n(E_1, \theta) = \frac{C_1 + C_2}{C_3} \tag{A.4}$$

$$C_1 = m_4(E_1 - Q)(m_n + m_4) - m_1 E_1(m_4 - m_n \cos(2\theta)) \tag{A.5}$$

$$C_2 = -2\cos(\theta)\sqrt{m_1 m_3 E_1(m_4(m_3 + m_4)(E_1 - Q) - m_1 E_1(m_4 + m_3 \sin^2(\theta)))} \tag{A.6}$$

$$C_3 = (m_n + m_4)^2 \tag{A.7}$$

The final step of eliminating the angle is achieved by substituting in the known masses, Q, and collision energy, then numerically integrating to average over all angles θ (all integration was carried out to a relative error of $<10^{-6}$. This results in a different relationship for each reaction.

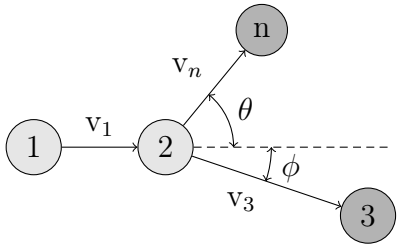

Figure A-1: Coordinate system used for inelastic scattering calculation of nucleus 1 colliding with nucleus 2 to produce a neutron and residual nucleus 3. The velocities shown relative to rest frame of particle 2.

Appendix B

Figures

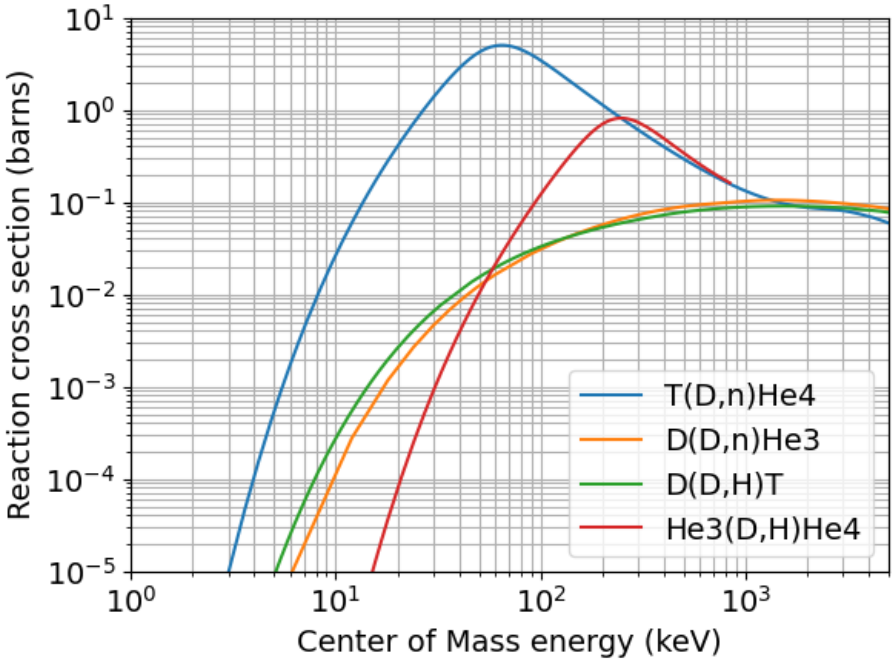

Figure B-1: Cross sections relevant to Deuterium-containing fuel mixes[6]. Values were assumed zero outside the energy ranges provided by ENDF library, and derived rates varied less than 1% when instead assuming value of nearest known cross section.

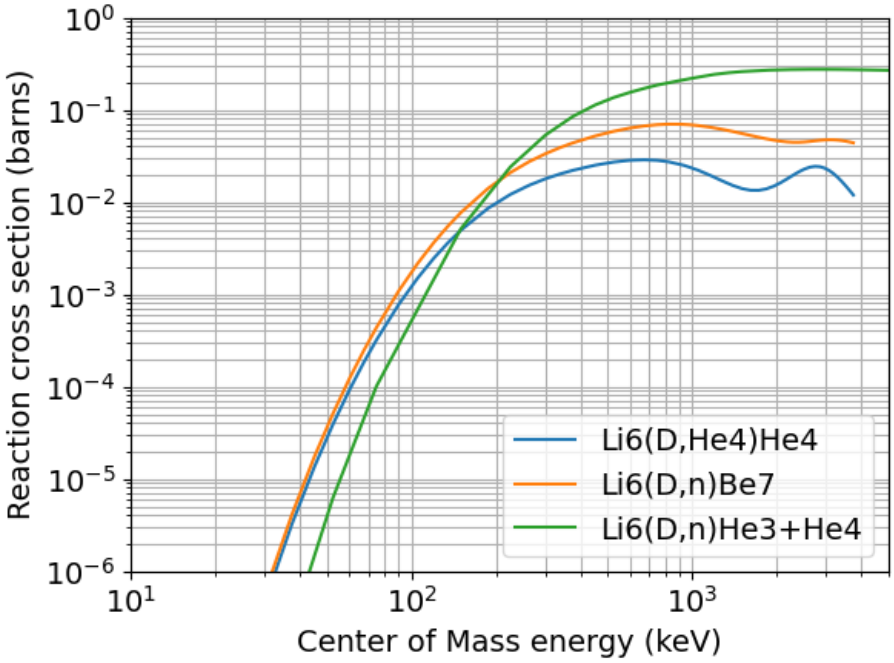

Figure B-2: Cross sections relevant to D-Li6 fuel mix[6]. Values were assumed zero outside the energy ranges provided by ENDF library, and derived rates varied less than 1% when instead assuming value of nearest known cross section.

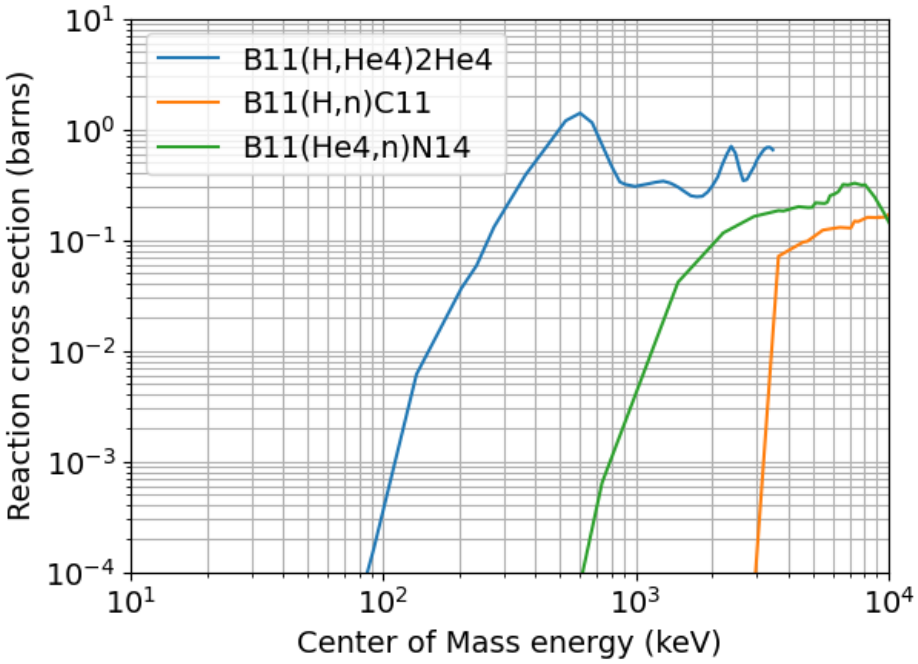

Figure B-3: Cross sections relevant to H-B11 fuel mix[6]. Values were assumed zero outside the energy ranges provided by ENDF library, or [14] for the alpha-producing reaction. Derived rates varied less than 1% when instead assuming value of nearest known cross section.

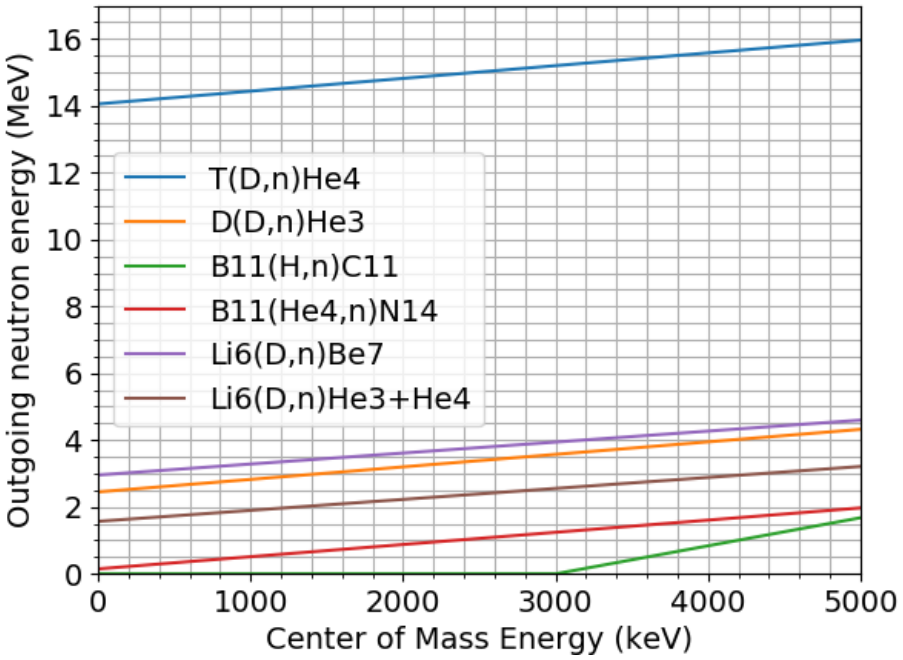

Figure B-4: Outgoing neutron energies relative to collision energy

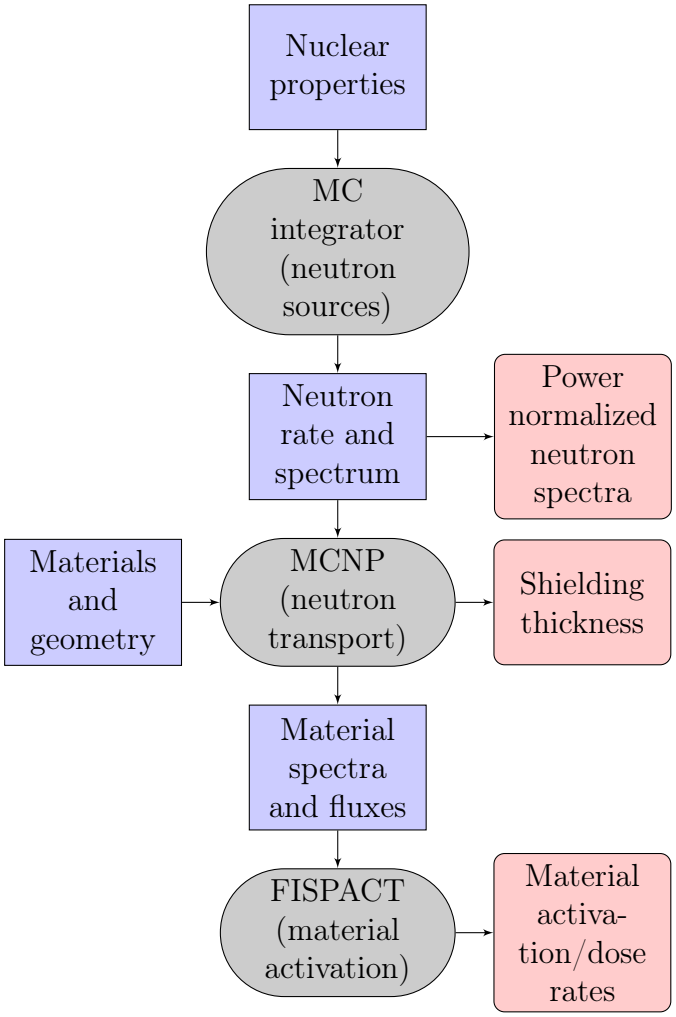

Figure B-5: Flow chart of computational model run per fuel type. Rectangular regions represent data, while elliptical regions represent algorithms/codes run on the data. The values directly quantifying radiological risk are represented by rounded boxes to the right.

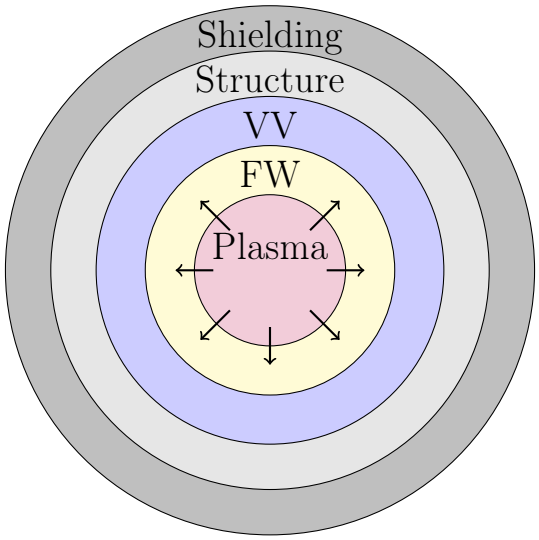

Figure B-6: Simplified reactor geometry used for attenuation and activation. Concentric spherical shells of plasma, first wall (FW), vacuum vessel (VV), and shielding. Neutrons are produced uniformly and isotropically in the plasma and propagate outwards. Regions not shown to scale.

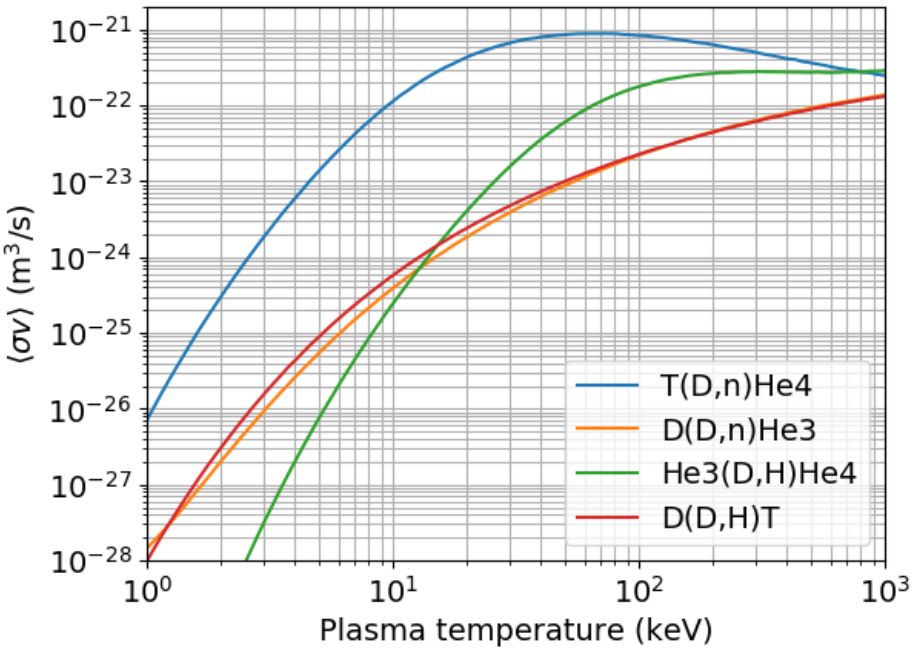

Figure B-7: $\langle\sigma v\rangle$-T curves relevant to all Deuterium-containing fuel mixes.

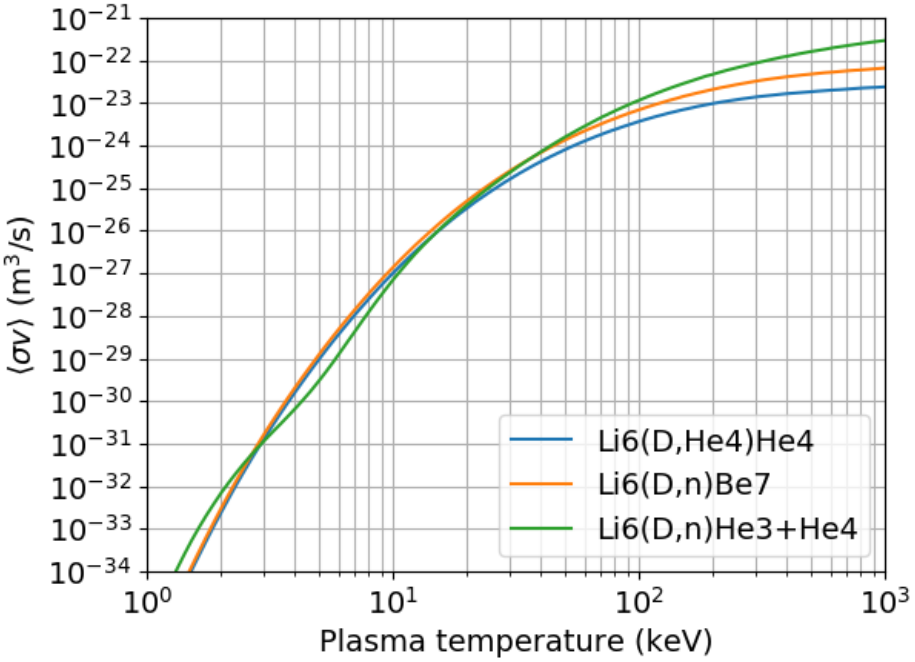

Figure B-8: $\langle\sigma v\rangle$-T curves relevant to D-Li6 fuel mix.

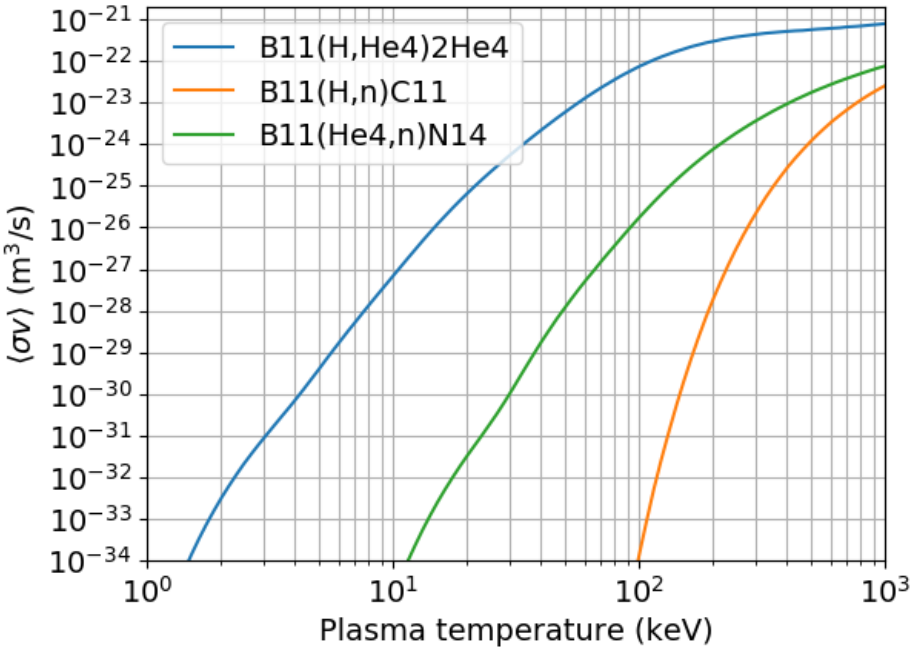

Figure B-9: $\langle \sigma v \rangle$-T curves relevant to H-B11 fuel mix.

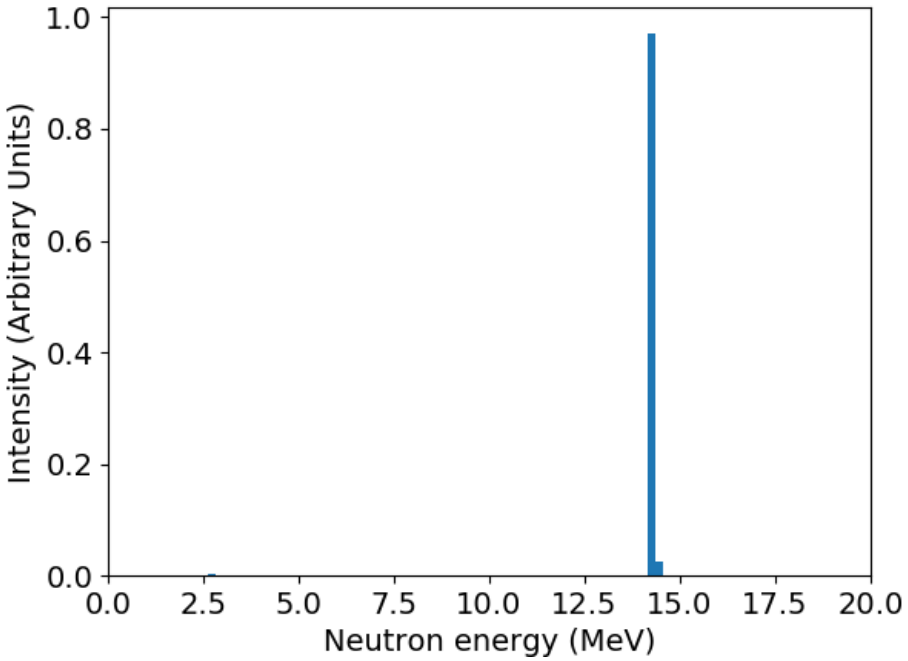

Figure B-10: Neutron spectrum from D-T plasma at 13keV.

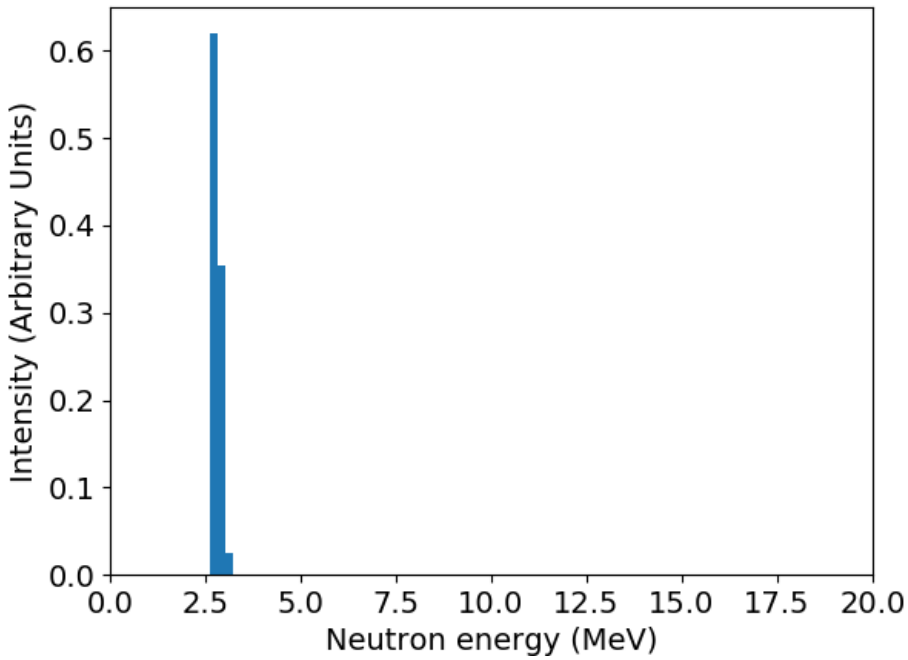

Figure B-11: Neutron spectrum from D-D and D-He3 plasmas at 70keV.

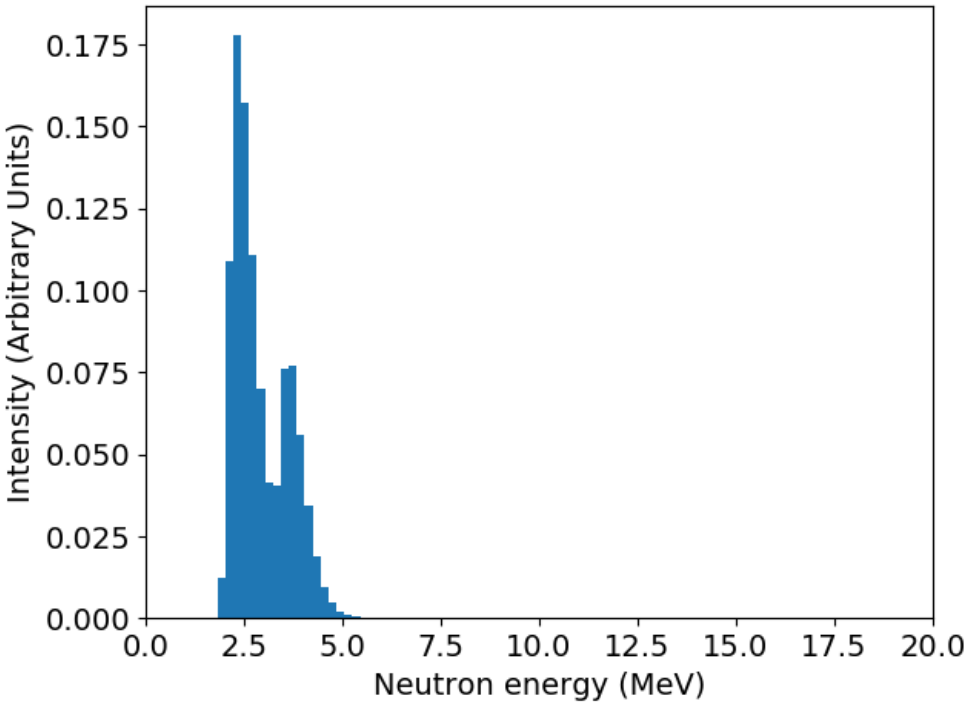

Figure B-12: Neutron spectrum from D-Li6 plasma at 300keV.

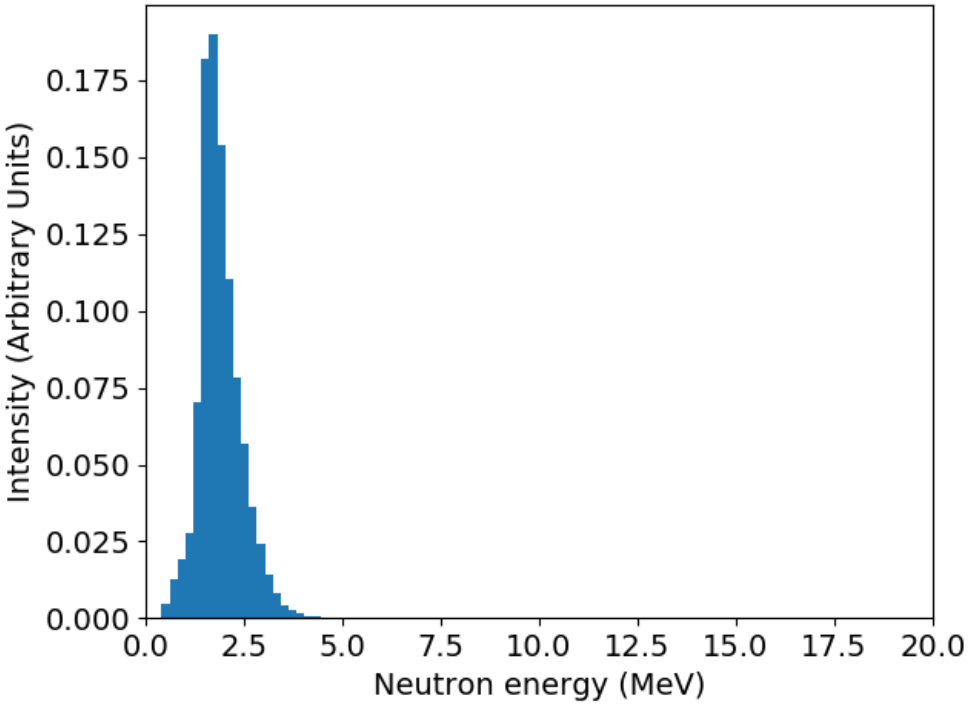

Figure B-13: Neutron spectrum from H-B11 plasma at 300keV.

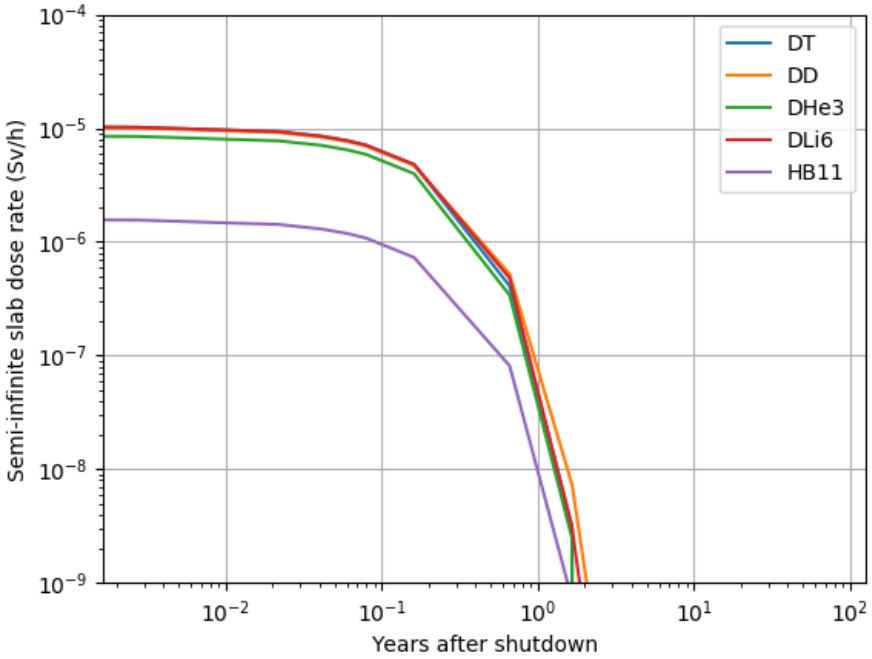

Figure B-14: Activation study of Boron Carbide first wall following 1 full power year at 500MWf.

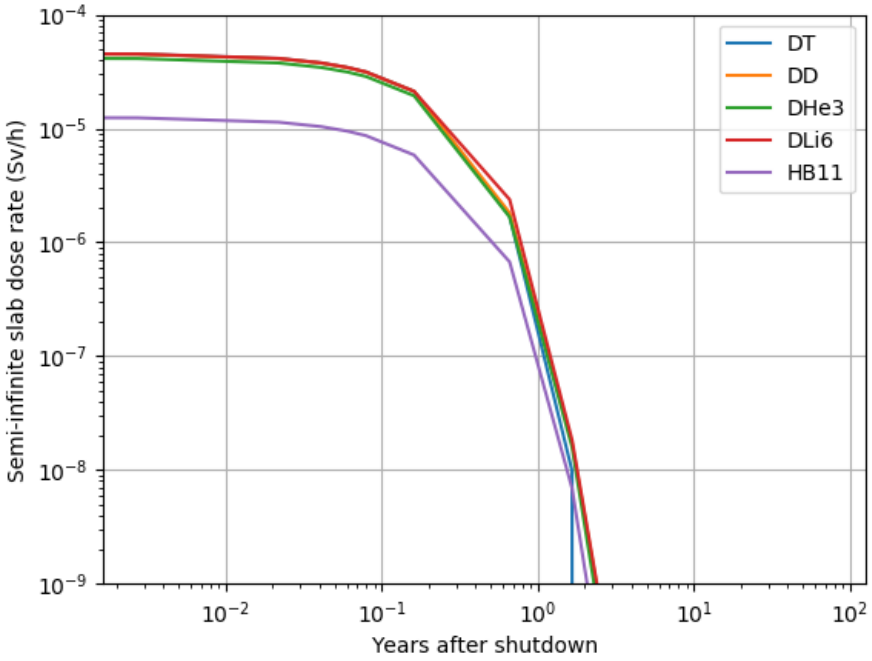

Figure B-15: Activation study of Graphite first wall following 1 full power year at 500MWf.

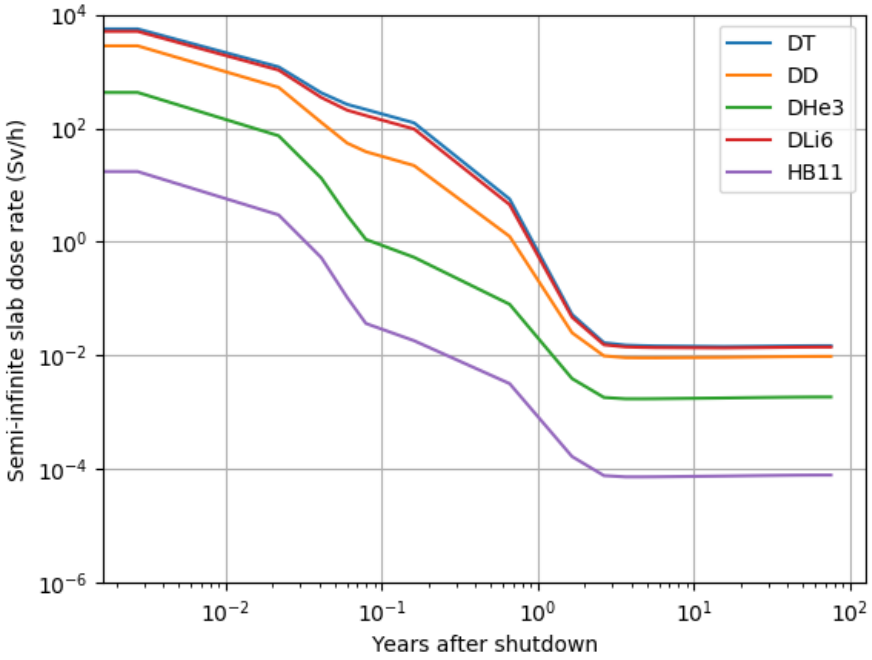

Figure B-16: Activation study of TZM first wall following 1 full power year at 500MWf.

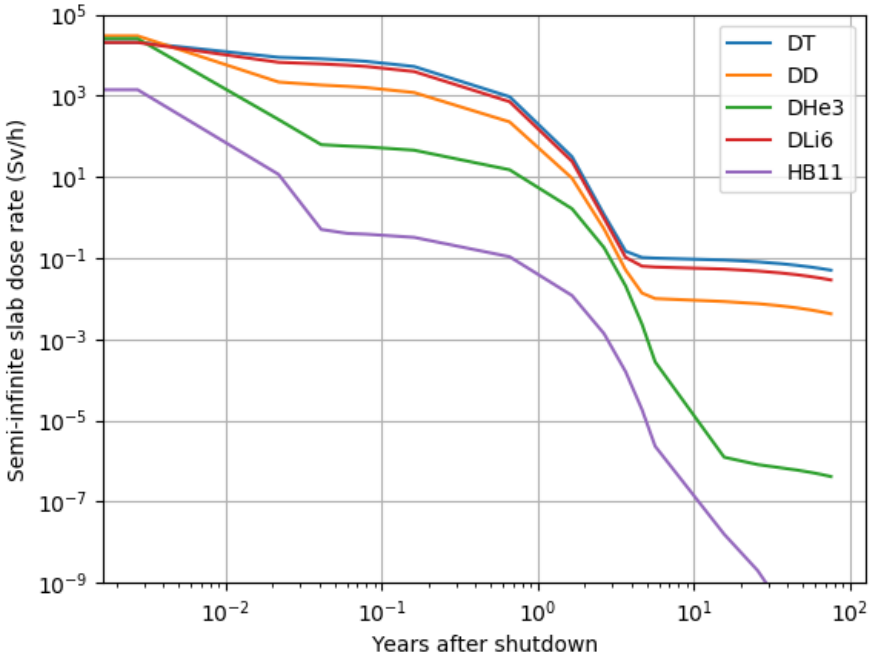

Figure B-17: Activation study of Tungsten first wall following 1 full power year at 500MWf.

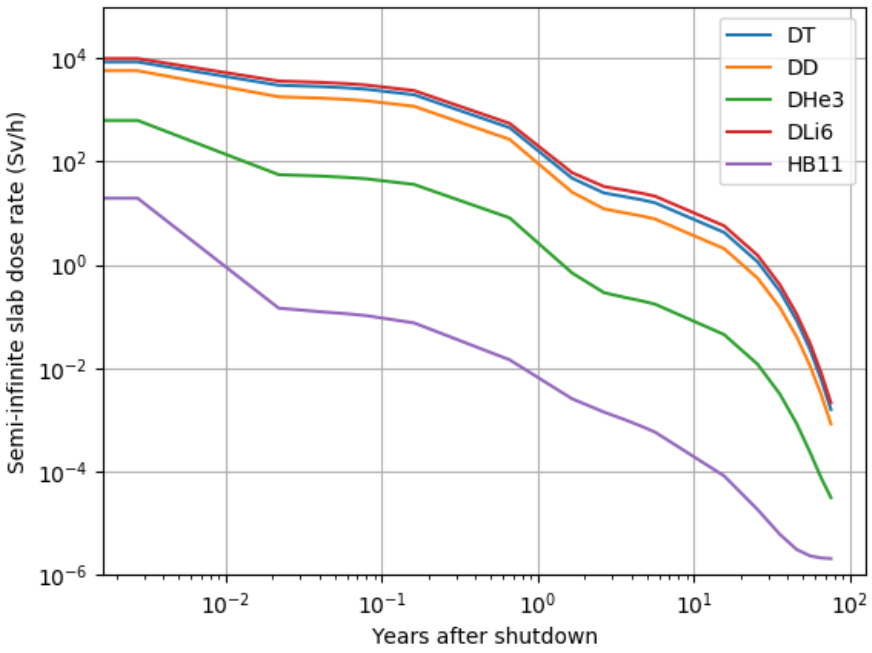

Figure B-18: Activation study of Inconel vacuum vessel with Boron Carbide first wall following 1 full power year at 500MWf.

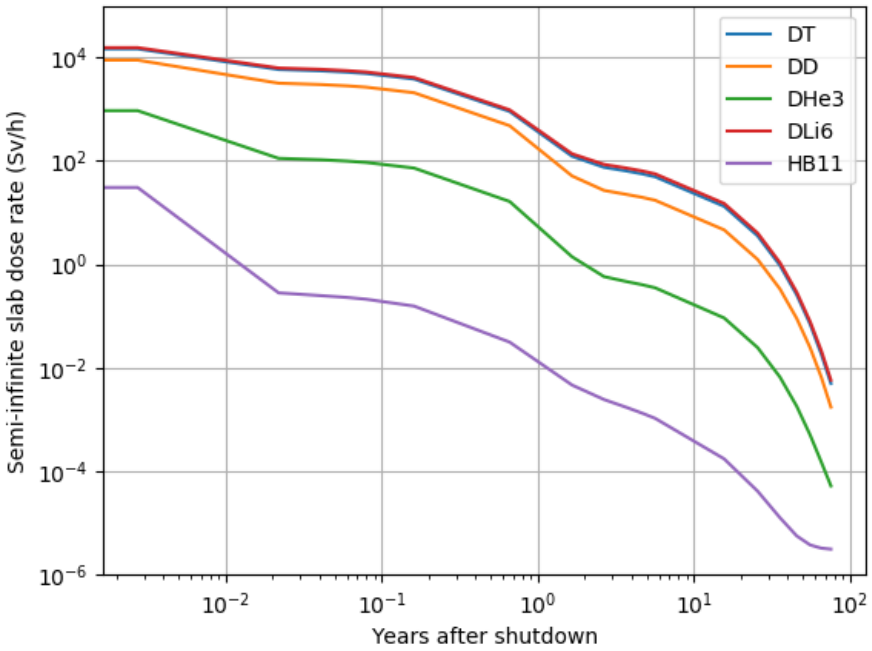

Figure B-19: Activation study of Inconel vacuum vessel with Beryllium first wall following 1 full power year at 500MWf.

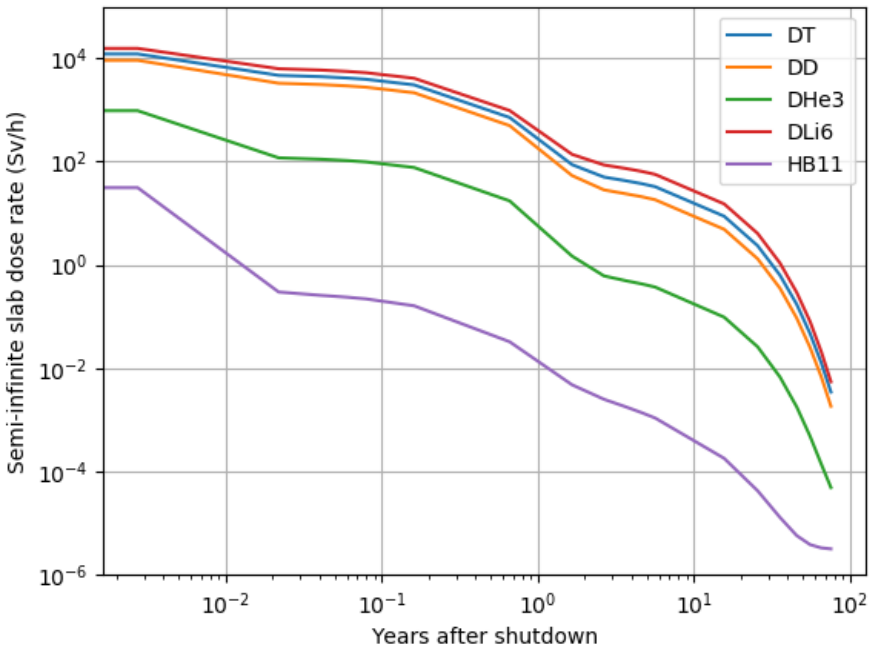

Figure B-20: Activation study of Inconel vacuum vessel with Graphite first wall following 1 full power year at 500MWf.

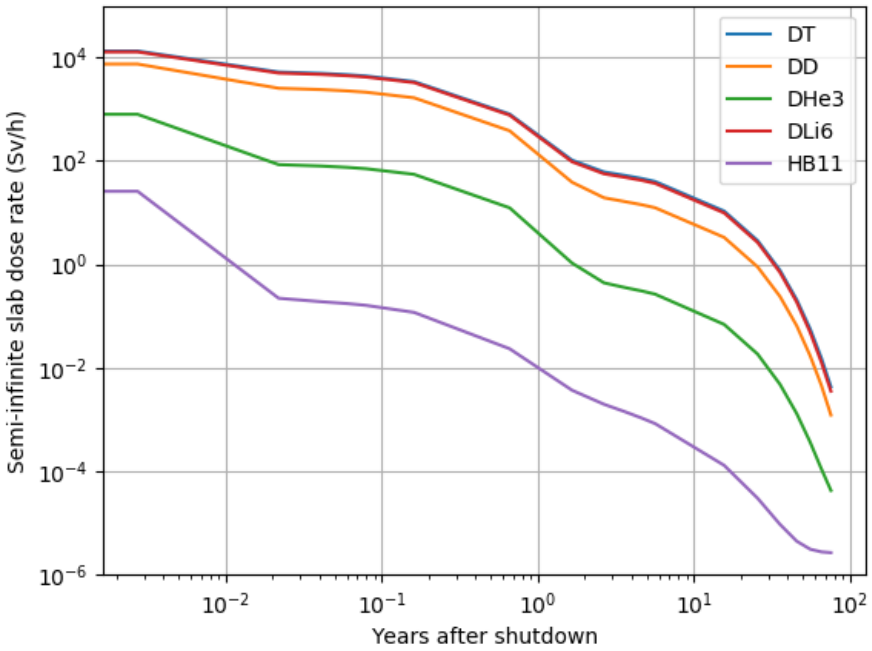

Figure B-21: Activation study of Inconel vacuum vessel with TZM first wall following 1 full power year at 500MWf.

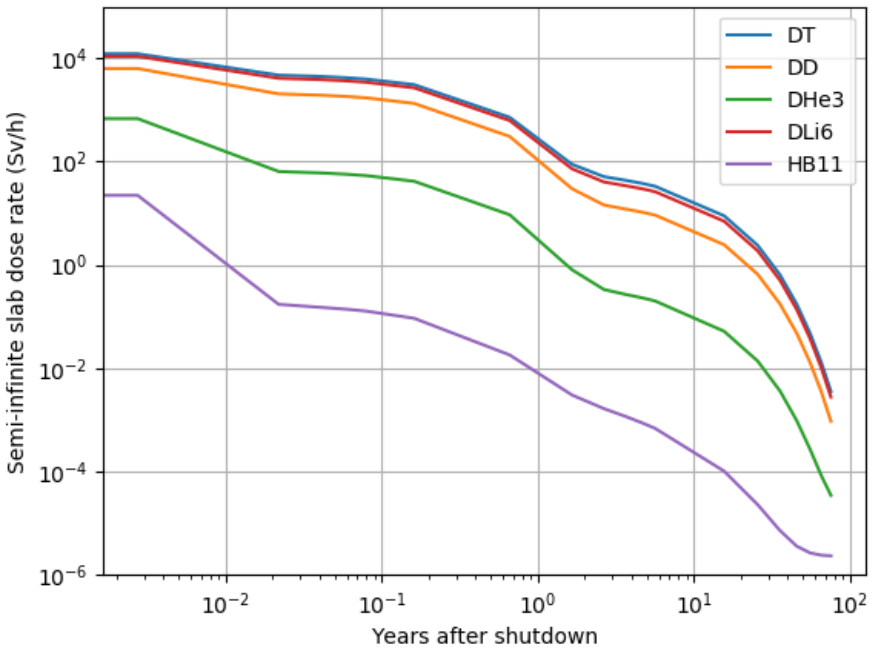

Figure B-22: Activation study of Inconel vacuum vessel with Tungsten first wall following 1 full power year at 500MWf.

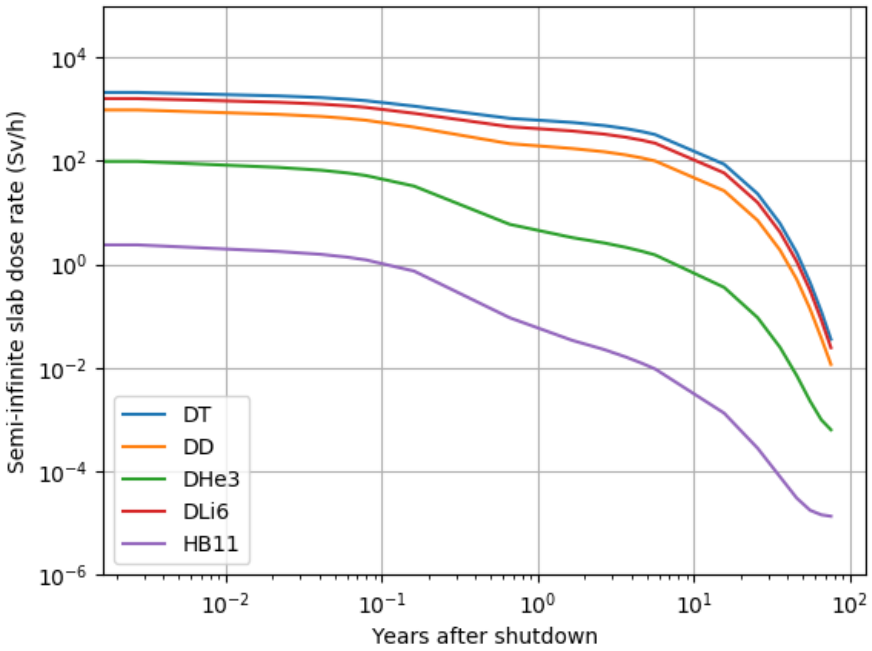

Figure B-23: Activation study of SS-316L structure with Boron Carbide first wall following 1 full power year at 500MWf.

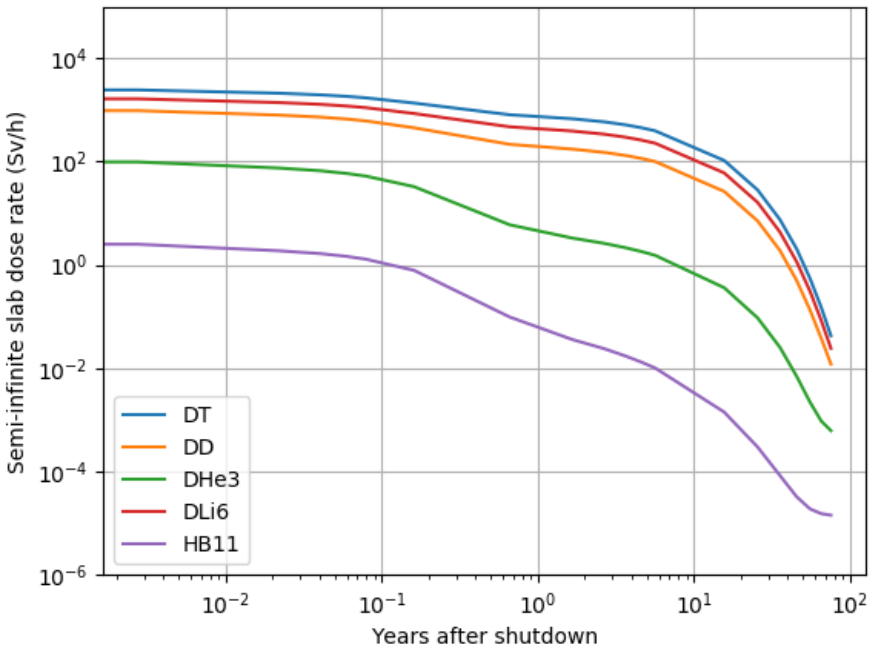

Figure B-24: Activation study of SS-316L structure with Beryllium first wall following 1 full power year at 500MWf.

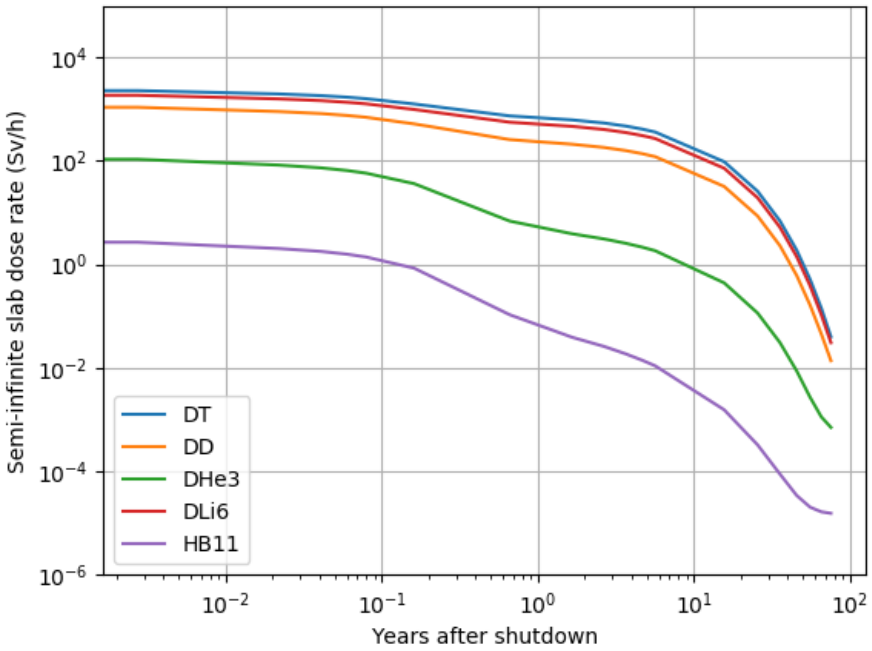

Figure B-25: Activation study of SS-316L structure with Graphite first wall following 1 full power year at 500MWf.

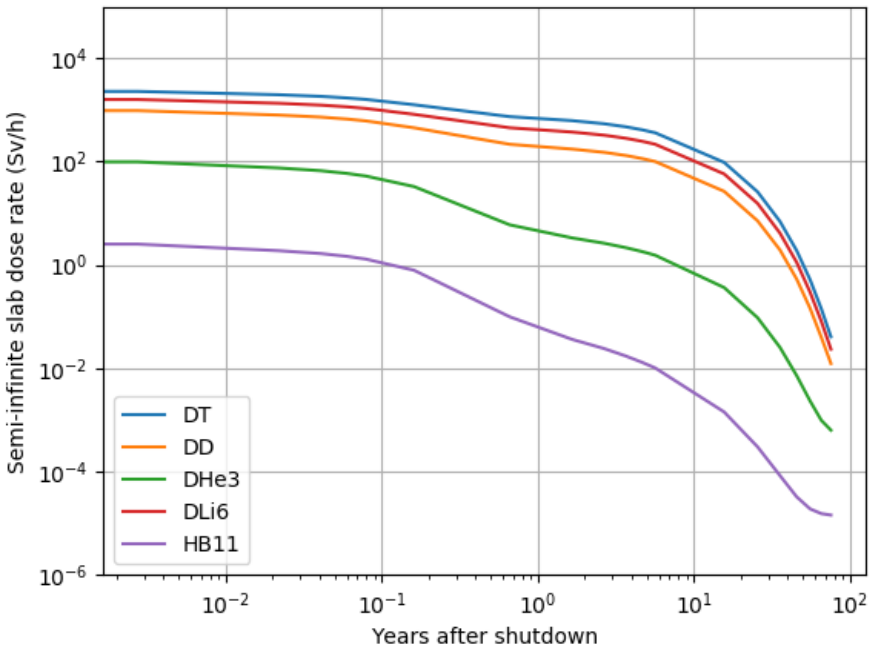

Figure B-26: Activation study of SS-316L structure with TZM first wall following 1 full power year at 500MWf.

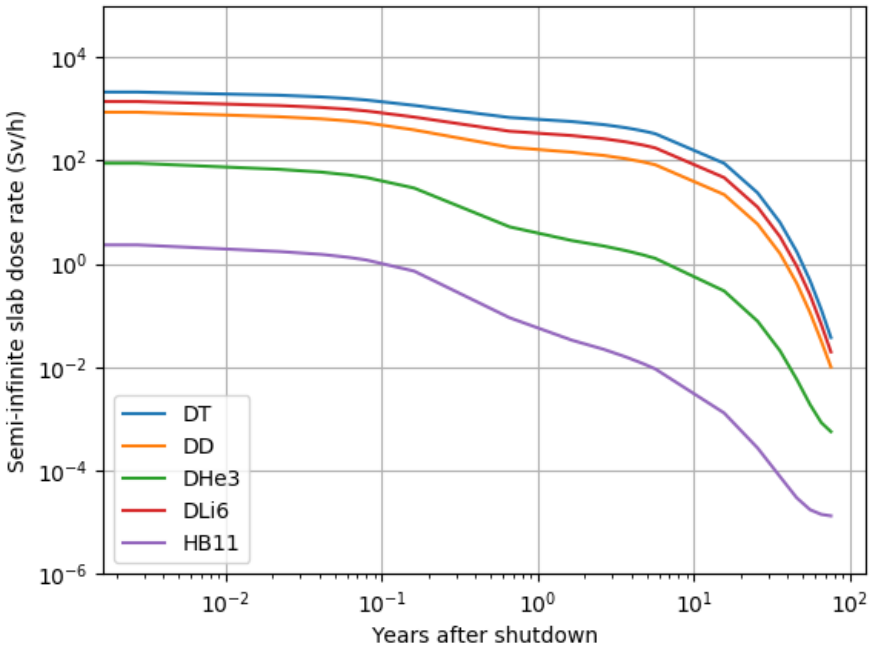

Figure B-27: Activation study of SS-316L structure with Tungsten first wall following 1 full power year at 500MWf.

Bibliography

[1] 10 C.F.R §20.1601.

[2] 10 C.F.R §20.1201.

[3] Neutron and Gamma-Ray Fluence-To-Dose Factors. 1991. American National Standards Institute.

[4] ITER Physics Basis Editors et al. ITER Physics Basis. *Nuclear Fusion*, 39, 1999.

[5] A.J Koning et al. TENDL-2017: TALYS-based Evaluated Nuclear Data Library. 2017. https://tendl.web.psi.ch/tendl2017/tendl2017.html.

[6] D.A. Brown et al. ENDF/B-VIII.0: The 8th Major Release of the Nuclear Reaction Data Library with CIELO-project Cross Sections, New Standards and Thermal Scattering Data. *Nuclear Data Sheets*, 2018.

[7] A. Creeley et al. Overview of the SPARC tokamak. *Journal of Plasma Physics*, 86, 2020.

[8] C.J. Werner et al. MCNP6.2 Release Notes. Report LA-UR-18-20808, Los Alamos National Laboratory, 2018.

[9] M.R. Gilbert M. Fleming, T. Stainer. The FISPACT-II User Manual. 2018.

[10] Seyed Mohammad Motevalli and Fereshteh Fadaei. A Comparison Between the Burn Condition of Deuterium–Tritium and Deuterium–Helium-3 Reaction and Stability Limits. *Zeitschrift für Naturforschung A*, 70:79–84, 2015.

[11] T.A. Oliphant, F.L. Ribe, and T.A. Coultas. Direct conversion of thermonuclear plasma energy by high magnetic compression and expansion. *Nuclear Fusion*, 13(4):529–532, aug 1973.

[12] S. Putvinski. pb11-reactor: trends and physics issues. Presentation, 2015.

[13] S. V. Putvinski et al. Fusion reactivity of the pb11 plasma revisited. *Nuclear Fusion*, 59, 2019.

[14] M. Sikora and H. Weller. A New Evaluation of the 11B(p,α)$\alpha\alpha$ Reaction Rates. *Journal of Fusion Energy*, 35:538–543, 2016.

[15] B. H. Smith, R. Burleigh, W. Dexter, and L. Reginato. Engineering study of the electrical design of a 1000-megawatt direct converter for mirror reactors. 1972.

[16] P. E. Stott. The feasibility of using D–3He and D–D fusion fuels. *Plasma Physics and Controlled Fusion*, 47:1305–1338, 2005.

[17] J. Ch. Sublet, J. W. Eastwood, J. G. Morgan, M. R. Gilbert, M. Fleming, and W. Arter. FISPACT-II: An Advanced Simulation System for Activation, Transmutation and Material Modelling. *Nucl. Data Sheets*, 139:77–137, 2017.

[18] Ralph G Williams, Christopher J Gesh, and Richard T Pagh. Compendium of material composition data for radiation transport modeling. Technical Report PNNL-15870, Pacific Northwest National Lab, Richland, WA, 2006.